Energy & Environmental Science

Cite this: *Energy Environ. Sci.*, 2011, **4**, 3632

www.rsc.org/ees

PAPER

A conceptual thermal actuation system driven by interface tension of nanofluids

Baoxing Xu,[a] Yu Qiao,[b] Taehyo Park,[c] Moonho Tak,[c] Qulan Zhou[d] and Xi Chen*[ace]

Received 3rd April 2011, Accepted 17th June 2011
DOI: 10.1039/c1ee01405f

In a system containing nanoporous materials and liquids, the well-known thermo-capillary effect can be amplified by the ultralarge specific surface area of the nanopores. With appropriate temperature change, the relative wetting–dewetting transition can cause the liquid to flow in or out of the nanopores, and part of the thermal energy is converted to significant mechanical output. A conceptual design of such a thermal actuation/energy conversion/storage system is investigated in this paper, whose working mechanism, *i.e.* the thermally dependent infiltration behaviors of liquids into nanopores, is analyzed using molecular dynamics simulations. The fundamental molecular characteristics, including the density profile, contact angle, and surface tension of the confined liquid molecules, are examined in considerable detail. The influences of pore size, solid phase and liquid species are elucidated, which couple with the thermal effect. The energy density, power density, and efficiency of the thermal actuation system are evaluated. An infiltration experiment on a zeolite/water system is performed to qualitatively validate these findings.

1. Introduction

The solid–liquid interface tension is responsive to thermal fluctuation. For example, for temperature variation associated with typical low grade heat ($\Delta T = 30$–$50\ ^\circ C$), the solid–liquid interface tension can vary by 20–50%, or on the order of 10–100 mJ m^{-2}. Such a variation, when multiplied by the ultralarge specific surface area of a nanoporous material ($A \approx 100$ to 2000 $m^2\ g^{-1}$), can lead to a significant energy conversion/storage and power output. As the relative wetting–dewetting transition occurs, the liquid molecules could enter into or be repelled out of the nanopores at a high speed, enabling a promising nano-propulsion system with considerable energy and power density. The conceptual design of such a thermo-capillary effect-based nanofluidic thermal actuation system is demonstrated in this paper using both atomistic simulations and experiments. Besides functioning as a thermo-machine, the similar system design may be employed for storage of low-grade heat with high energy density.

The proposed energy conversion/actuation functionalities are underpinned by the fundamental behaviors of nanofluids, whose unique characteristics have also motivated the development of other types of nanofluidic devices including energy storage/conversion/transport systems,[1–4] ion/molecule filters,[5–7] nanofluidic transistors,[8] and nanofluidic pumps,[9,10] among others.

[a]*Columbia Nanomechanics Research Center, Department of Earth and Environmental Engineering, Columbia University, New York, NY, 10027, USA. E-mail: xichen@columbia.edu*
[b]*Department of Structural Engineering, University of California – San Diego, La Jolla, CA, 92093-0085, USA*
[c]*Department of Civil & Environmental Engineering, Hanyang University, Seoul, 133-791, Korea*
[d]*State Key Laboratory of Multiphase Flow in Power Engineering, Xi'an Jiaotong University, Xi'an, 710049, China. E-mail: qlzhou@mail.xjtu.edu.cn*
[e]*SV Lab, School of Aerospace, Xi'an Jiaotong University, Xi'an, 710049, China*

Broader context

Improving the efficiency of energy conversion represents a paramount challenge in view of the urgent demand for energy and environmental sustainability. As a new approach of energy conversion, nanofluidic devices enable the flexible control of mass transfer and energy transfer at the nanoscale, and the energy density is boosted by the ultralarge specific surface area of the nanoporous material. Here, we propose a thermal-to-mechanical energy conversion system enabled by nanofluids. The infiltration and defiltration barriers of liquids flowing in and out of nanopores are a function of temperature, which is employed to control the actuation system. The working principle of the thermally responsive interfacial tension-driven actuation system is explored using molecular dynamic simulations and experiments. High power density, energy density, and efficiency are demonstrated. The energy conversion system can become a high density thermal storage device.

With regard to the thermal characteristics, temperature gradient has been proven as an effective technique for driving fluid flows in nanochannels.[10,11] For example, Liu and Li proposed a composite nanochannel system, where half of the channel was of low surface tension and the other half has a relatively higher surface tension,[10] and their molecular dynamics (MD) simulations showed that fluids can be continuously driven by a symmetric temperature gradient. Longhurst and Quirke's MD simulations demonstrated continuous pumping of fluid through carbon nanotubes,[12] where the fluid contained in a heated reservoir could be ejected subsequently from the hot end of the tube. By suspending nanoporous particles in liquids, Qiao *et al.* developed a thermally controllable nanoporous spring[13] and a volume-memory liquid[14] based on the thermo-capillary effect. Jiao *et al.* studied on the thermally induced actuation of liquid droplet in a micro-channel[15] where the driving force (temperature gradient) was provided by four heaters at the channel ends. Nguyen designed an integrated heater and temperature sensor to control the droplet formation process, and thermally adjusted the droplet diameter to over two times of its original value.[16]

Despite these previous efforts, manipulating liquid motions in nanochannels still represents an enormous challenge, largely due to the lack of understanding of the molecular mechanisms of the thermal response of liquid infiltration and transport in nanopores. These features can be clarified using atomistic simulations, and the effective thermo-capillary effects may be depicted *via* the explorations of the fundamental fluidic parameters (*e.g.* contact angle, surface tension, *etc.*) in a confined nanoenvironment. A systematic study on the thermal sensitivity of the effective wettability with respect to different pore sizes, pore phase and liquid species may further benefit the optimization of the nano-propulsion system, in terms of performance indices such as energy density, power density, and thermal efficiency.

The present study employs MD simulations to reveal the fundamental thermal-dependence of the infiltration characteristics of liquid molecules into hydrophobic nanopores, and the underlying molecular mechanisms are elucidated. Based on the variation of the effective solid–liquid interfacial tension on temperature, a conceptual thermally responsive energy conversion system (also referred to as thermal machine, propulsion, or thermal actuation system in this paper) is proposed. The performance indices are obtained using MD simulations, which demonstrate that the liquids can be continuously pumped in and out of nanopores by adjusting the system temperature. The study may shed some insights on the designing of similar nanofluidic devices for actuation, thermal storage, and energy conversion.

2. Model and computational method

The computational cell consists of a model nanochannel (*e.g.* a single-walled carbon nanotube, CNT) and a reservoir with model liquid (*e.g.* water), Fig. 1, and periodical boundary condition is imposed on the four lateral planes of the computational cell. One end of the nanotube is closed, and the open end is

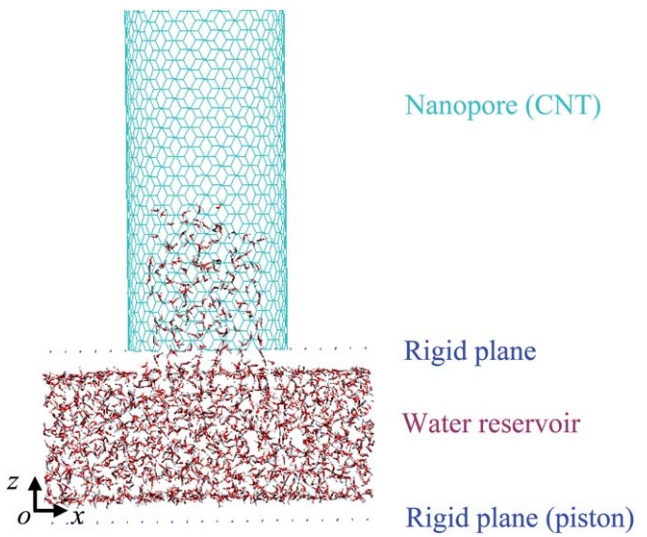

Fig. 1 The MD computational cell of the model nanopore/liquid system. One end of a long nanotube is inserted into a liquid reservoir, and the other end is closed. The water reservoir is bounded with a fixed upper plane and movable bottom plane. An external pressure is applied on the piston-like bottom plane. Periodical boundary condition is imposed to the four lateral planes of the cell.

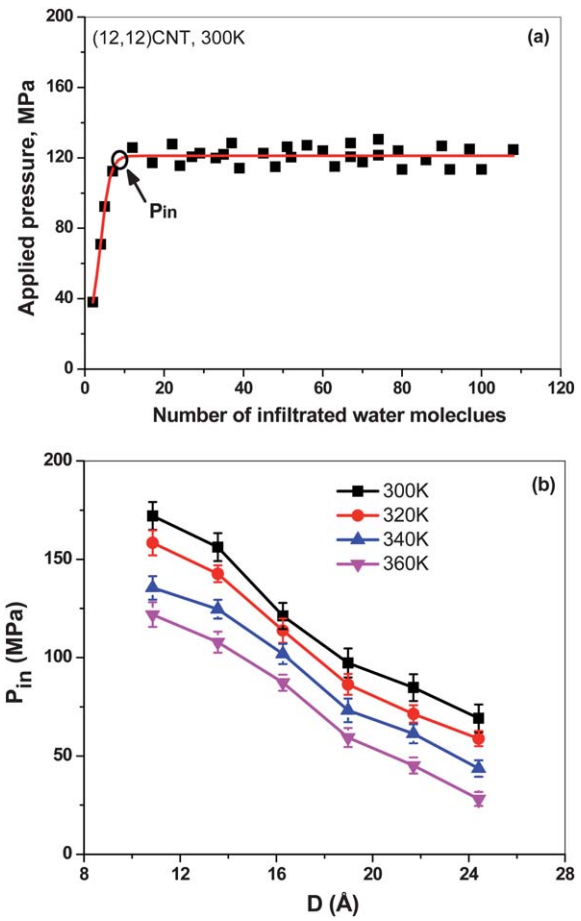

Fig. 2 (a) Variation of the number of infiltrated water molecules into a (12,12) CNT as a function of the applied quasi-static pressure (at the temperature of 300 K). From the plateau of the infiltration curve, the critical infiltration pressure, P_{in}, can be deduced; (b) The effect of the CNT diameter, D, and temperature, T, on the critical infiltration pressure, P_{in}.

inserted into the reservoir. The reservoir is bounded by two rigid planes, with the upper one fixed and the bottom plane acts like a piston and is moveable in the axial direction.

MD simulations are carried out using LAMMPS.[17] The initial water molecule density in the reservoir is close to that of bulk water, $\rho_0 = 998.0$ kg m^{-3} at 300 K and 1 atm. Since the effect of CNT flexibility is small on the infiltration behavior,[18] the CNT is treated as a rigid channel. The steric and van der Waals (vdW) carbon–carbon interaction is accounted for by employing the 12-6 Lennard-Jones (L-J) potential, $U(r_{ij}) = 4\varepsilon[(\sigma/r_{ij})^{12} - (\sigma/r_{ij})^{6}]$, where r_{ij} denotes the distance between atoms, and ε and σ are the energy and length parameters, respectively. The water is modeled by the rigid extended Simple Point Charge potential SPC/E,[19] which consists of a Coulomb potential between partial point charges on the oxygen and hydrogen atoms and an L-J potential between oxygen atoms; a cutoff distance of 10 Å is chosen.[20] The P3M (Particle–Particle Particle-mesh) technique with a root mean square accuracy of 10^{-4} is employed to handle the long range Coulomb interactions among water molecules. The carbon–water interaction is described by the L-J potential whose parameters are obtained from the experimental low-coverage isotherm data of oxygen adsorption on graphite.[21] By using these molecular models and parameters, the inner surface of CNT is ensured to be non-wetting to water and an external pressure is required for infiltration. As alternative solid and liquid phases, silica nanotube and NaCl/water solution are also chosen, whose force fields as well as the interaction with water molecules are described in similar fashion, ref. 22.

The system pressure can be adjusted by moving the piston, either quasi-statically or dynamically. By sampling a region near the entrance of CNT, the instantaneous effective applied pressure, P, is calculated based on the intermolecular potential among water molecules through the virial expression, $P = N'k_BT/V + \sum_i^{N'} r_i f_i/3V$, where N' is the number of water molecules inside the sampling region, k_B is the Boltzmann constant, T is the water temperature, V is the volume of sampling region, and the second term describes the contribution from the pairwise body interaction among the N' water molecules. V is taken to be sufficiently large to insure a nearly isotropic density distribution of water. At each time step, the information of atoms/molecules inside the sampling region is collected to calculate the instantaneous effective pressure. The Nose/Hoover thermostat with a damping parameter of 0.1 is employed to regulate the desired water temperature, which is a main variable in this paper.

3. Results and discussion

3.1. Fundamental infiltration behavior and thermal dependence

We first explore the fundamental quasi-static infiltration behavior of water molecules into a representative (12,12) CNT. Fig. 2a shows the variation of the number of intruded water molecules with applied pressure at the temperature of 300 K. When the pressure reaches a critical infiltration pressure, $P_{in} =$ 121 MPa in this case, a large number of water molecules start to invade the CNT after the capillary resistance (which is related to the solid–liquid interfacial energy) is overcome. Afterwards, the infiltration plateau remains quite flat, suggesting that the inner surface of CNT is quite smooth and the "frictional" dissipation is

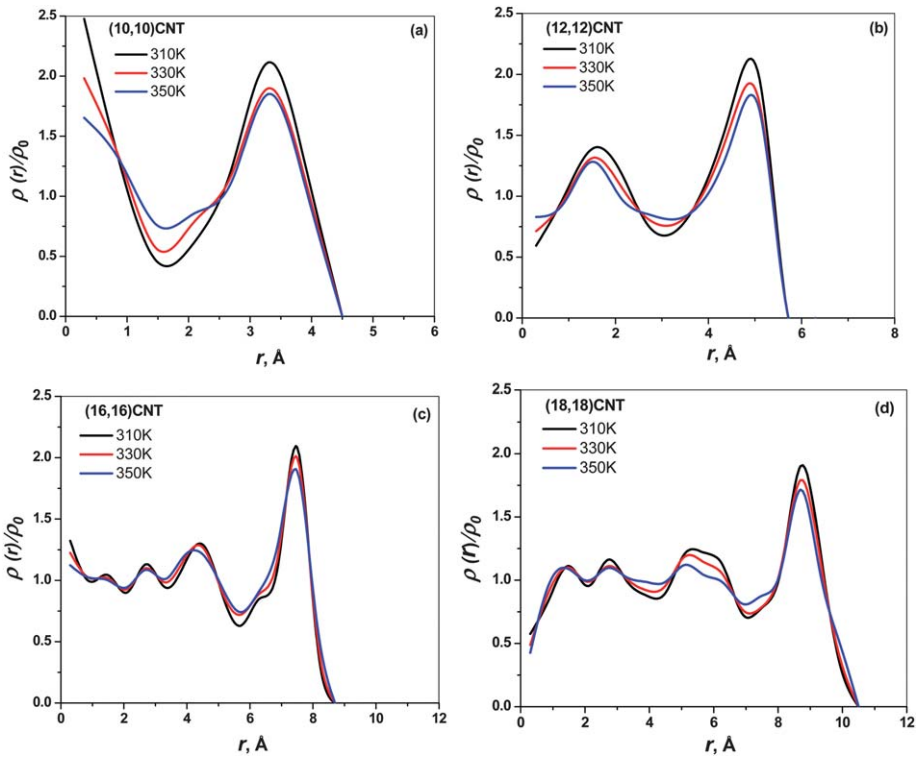

Fig. 3 (a) The normalized density profile distribution of water, $\rho(r)/\rho_0$, in the confined CNT along the radial direction, as the temperature is elevated. $\rho_0 = 998.0$ kg m^{-3}. (a) (10,10) CNT; (b) (12,12) CNT; (c) (16,16) CNT; (d) (18,18) CNT. The left and right axes are aligned with the tube axis and inner surface, respectively.

very small.[23] At different temperatures, the thermal dependence of the infiltration pressure is given in Fig. 2b, which is also coupled with the pore size effect. It is seen that the system becomes relatively more hydrophobic (with higher P_{in}) when the pore gets smaller or when the temperature is cooler, and that is largely related to the enhancement of the interfacial tension between solid and liquid. The molecular mechanism in the confining nanoenvironment is discussed next.

3.2. Underlying molecular mechanism

During quasi-static infiltration, the equilibrium between the applied pressure and the imbibing pressure of water into CNT can be described by the classic Laplace–Young's equation, $P_{in} = -4\gamma\cos\theta/D$, where γ is the surface tension of water molecules, θ is the contact angle of the confined water molecules, and D is the accessible diameter of water molecules inside the CNT. This equation has been validated at the nanoscale by incorporating size effects of involved parameters[24]—note that, in Fig. 2b P_{in} does not vary with pore diameter as $1/D$, this implies that both γ and θ are size-dependent. If the system is warmer, as will be shown below, both γ and θ reduce significantly yet D enlarges slightly, leading to the observed reduction of P_{in}.

First, some qualitative insights of the confined liquid molecules can be learned from their average radial density distributions in Fig. 3, where the CNT radius is also varied. The fluctuations indicate that the water molecules form a layered structure, and the interaction is the most prominent in the first solvation shell (FSS) near the tube wall. With the increase of CNT diameter, the smaller fluctuations imply that the water molecules become more cohesive and the water–CNT interaction is weaker, which reduces the infiltration threshold. As temperature rises, the position of FSS moves closer to the tube wall which helps to increase the effective D, and contributes to a small part of the reduction of P_{in}. Meanwhile, the amplitude of FSS is decreased and that suggests the effective interfacial tension ($\gamma\cos\theta$) is reduced.

Next, we quantify the contributions of γ and θ. The contact angle can be determined from an independent analysis by following Werder *et al.*[25] For liquid molecules confined in a cavity, at the equilibrium state the spatial positions of the molecules at the meniscus front are averaged over a long computational time, and from such an averaged meniscus profile the contact angle can be deduced, illustrated in the inset of Fig. 4a. Fig. 4a also shows the variation of θ with temperature and two different pore sizes, which indicate that the contact angle is smaller in a warmer system or in a smaller pore, consistent with experimental results.[13] The current result of contact angle is also close to that calculated by Werder *et al.*,[25] and the small difference is due to the different water molecule model and CNT flexibility. Based on the values of θ (Fig. 4a) and P_{in} (Fig. 2b), from the Laplace–Young's equation, the surface tension γ can be calculated (Fig. 4b), which shows a decreasing trend in a warmer system or a larger pore. Thus, the thermal dependences of γ and θ are primarily responsible for the relative wetting transition of the nanochannel, as the temperature varies.

3.3. Variation of solid and liquid phases

The analyses above are based on the model CNT/water system. Apparently, when different solid and liquid phases are employed,

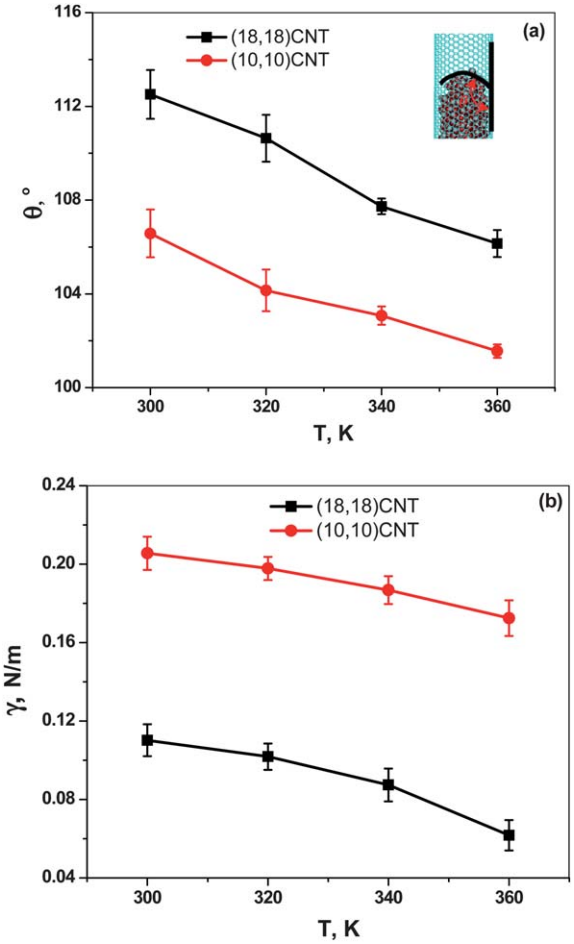

Fig. 4 Thermal variation of (a) contact angle, θ, of the confined water inside CNT; and (b) surface tension, γ. The CNT size is also varied.

the interfacial tension and thus the infiltration characteristics also vary. A substitute silica nanotube (SNT) with $D = 24.56$ Å, whose size matches with that of a (18,18) CNT, and a substitute liquid phase, NaCl/water solution of concentration 2.0 mol L^{-1}, are explored in this section. Partial charges of 0.89 e and −0.445 e are imposed on each silicon and oxygen atom, respectively, and the SNT is neutral overall.

Following the same quasi-static simulation procedure, Fig. 5a plots the variation of P_{in} as a function of temperature. Upon the same T, the P_{in} in SNT/water or CNT/NaCl solution system is slightly higher than that in the CNT/water system, implying stronger solid–liquid interactions. The corresponding contact angle, θ, and surface tension, γ, are given in Fig. 5b and c, respectively. To infiltrate the NaCl-solution, an extra work is needed to break the hydration shell, and thus P_{in} is higher compared with that of pure water. For SNT, the solid–liquid interaction is stronger than the CNT system, owing to the partially charged surface of SNT and polar water molecules, and therefore its infiltration process requires a larger work. The similar findings have been reported for fluidic transport in nanochannels,[22] which may provide a feasible strategy of improving the energy absorption capacity of nanofluidic devices/systems.

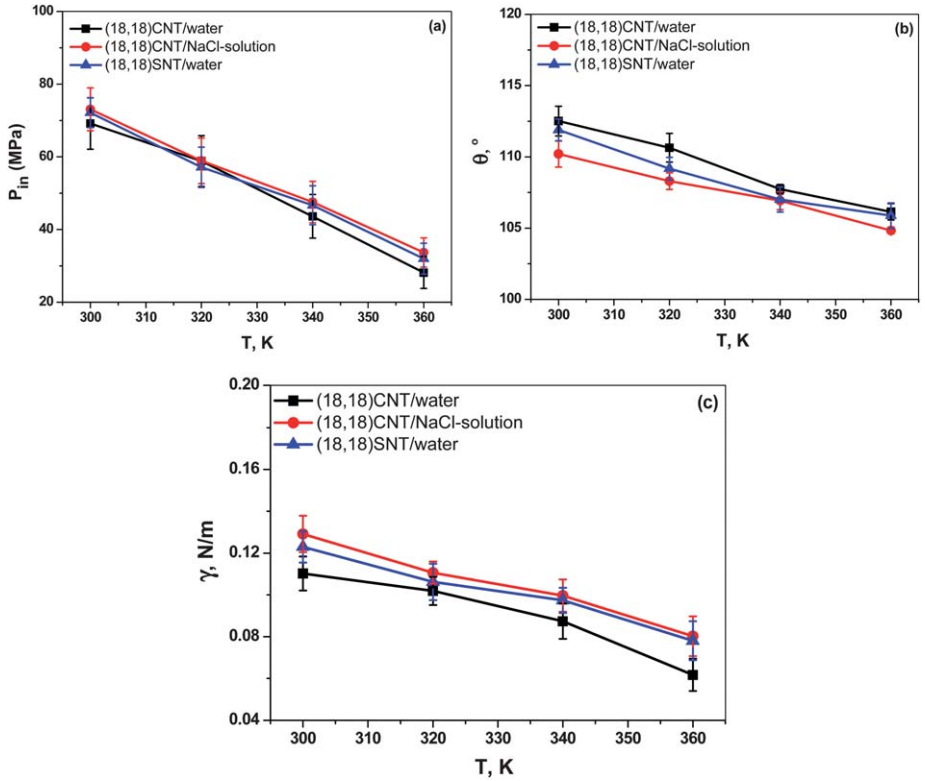

Fig. 5 The thermally dependent infiltration characteristics of different solid/liquid systems (a) infiltration pressure, P_{in}; (b) contact angle, θ; (c) surface tension, γ.

3.4. A conceptual thermal actuation system

For a nanoporous material with given pore size immersed in a non-wetting liquid, the infiltration pressure decreases monotonically with the increase of temperature, which enables a thermally controlled fluidic actuation system. Denote $P_{in}^{T_0}$ and $P_{in}^{T_1}$ as the critical infiltration pressure under T_0 (ambient temperature) and T_1 (elevated temperature), respectively. We apply a fixed external pressure P_{app} on the piston throughout the actuation/propulsion process, with $P_{in}^{T_1} < P_{app} < P_{in}^{T_0}$. When the working temperature is T_1, liquid intrudes into the nanopores and the system volume is reduced, and part of the thermal energy is converted to mechanical energy. When the system temperature returns to T_0, the nanopore becomes relatively hydrophobic and the liquid molecules defiltrate from the nanopores, thus part of the excessive interfacial energy is converted to mechanical work. Both processes are similar to that of a thermal machine, except that the present model is driven by the thermo-capillary effect of nanofluids.

In practice, one may employ two strategies to set P_{app}: the first one is to make P_{app} just below $P_{in}^{T_0}$, and the second one is to make P_{app} just above $P_{in}^{T_1}$. The first approach is applicable to a wide range of working temperature T_1, and when T_1 is higher the output work and power are larger. The second strategy works for a fixed working condition (pre-designed) T_1 in a quasi-static manner. In this study, we only focus on the first strategy (with T_0 = 300 K) and evaluate its output work, power, as well as thermal efficiency.

The actuation system is first illustrated using a representative (18,18) CNT/water system, where the length and diameter of the CNT are 4.9 nm and 2.4 nm respectively, and the reservoir (58 Å × 58 Å × 20 Å) initially contains 2312 water molecules. The piston position is adjusted *in situ* during the dynamic infiltration/defiltration processes, such that P_{app} is fixed as a constant just below P_{in}^{0}. When the system temperature is elevated, the water molecules enter the CNT (Fig. 6). The higher the temperature, the higher the infiltration flow rate (driven by the pressure difference, $P_{app} - P_{in}^{T_1}$). When the system is cooled to ambient temperature, the confined water molecules defiltrate at a rate slower than infiltration.

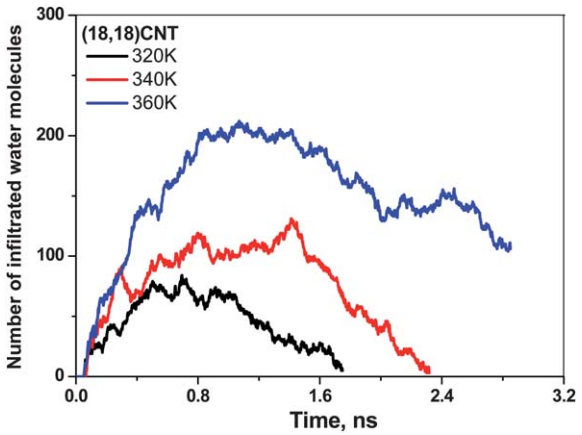

Fig. 6 For a representative themo-actuation system with (18,18) CNT and water, under a fixed P_{app}, the water molecules continuously invade into the tube with the increase of temperature. Water starts to flow out of the CNT 0.8 ns after the temperature is reduced to ambient.

During the infiltration process, the effective work output can be calculated as $W_{eff} = P_{app}\Delta V$, where ΔV is the volume reduction of the reservoir. The work reaches a maximum W_{max} when the CNT is filled up. Since the constraining effect of water molecules is different at different T (Fig. 3), W_{max} varies slightly with temperature. For the current model (18,18) the CNT/water system with specified dimensions, Fig. 7a, gives its maximum energy density (W_{max} per mass of the entire system), which is on the order of 10 J g^{-1} and much higher than conventional actuation materials such as shape memory alloys.

The second performance index of the actuation system is its power density (P per mass during infiltration), which is almost a constant during infiltration. Due to the strong dependency of the flow rate with the temperature difference, the average power density is a function of ΔT, as shown in the down triangle curve in Fig. 7b for the representative (18,18) CNT/water system.

The system's thermal efficiency can be estimated as $\eta = W_{eff}/(W_{eff} + W_T) \times 100\%$, where the total consumed thermal energy (W_T) can be estimated *via* the temperature variation and specific heat capacity of the system (note that for the low grade heat or small temperature variation considered herein, one may assume that the specific heat capacity is invariant with respect to temperature or pressure). Fig. 7c gives the efficiency of the (18,18) CNT/water system (down triangle curve). The system efficiency is enhanced at higher temperature due to the more pronounced reduction of the solid–liquid interaction.

3.5. Parametric study of the thermal actuation system

In terms of the performance indices (maximum energy density, power density, and efficiency), a parametric study can be carried out to obtain some insights on improving the system performance. First, we explore the pore size effect: as the CNT diameter is changed, we keep the ratio between the pore volume and reservoir volume a constant. Fig. 7 shows that with the help of the higher surface-to-volume ratio and stronger carbon–water interfacial tension, in general a smaller CNT can lead to better performance indices. Nevertheless we caution that if the CNT size is too small such that the infiltrated water molecules form a single-file[22,27] the system performance may decrease. Our study indicates an optimum pore size of about 1 nm, which may be achievable as high-density nanopore arrays in practice.[28–30]

Likewise, one may also adjust the liquid and solid phases. When the water phase is replaced by a 2.0 mol L^{-1} NaCl-solution while the same (18,18) CNT is employed, although the system mass is increased, the stronger solid–liquid interaction (Fig. 5) renders an increase in the energy density, power density, and efficiency. When the CNT is replaced by a SNT of same diameter while keeping the same water phase, despite the stronger SNT–water interaction (Fig. 5), SNT is considerably heavier than CNT, leading to lower energy and power densities in the present study. A more systematic parametric investigation may be carried out in future to optimize the material and system parameters, such as the pore phase, pore structure, surface treatment, liquid phase, liquid concentration, temperature variation rate, *etc.*

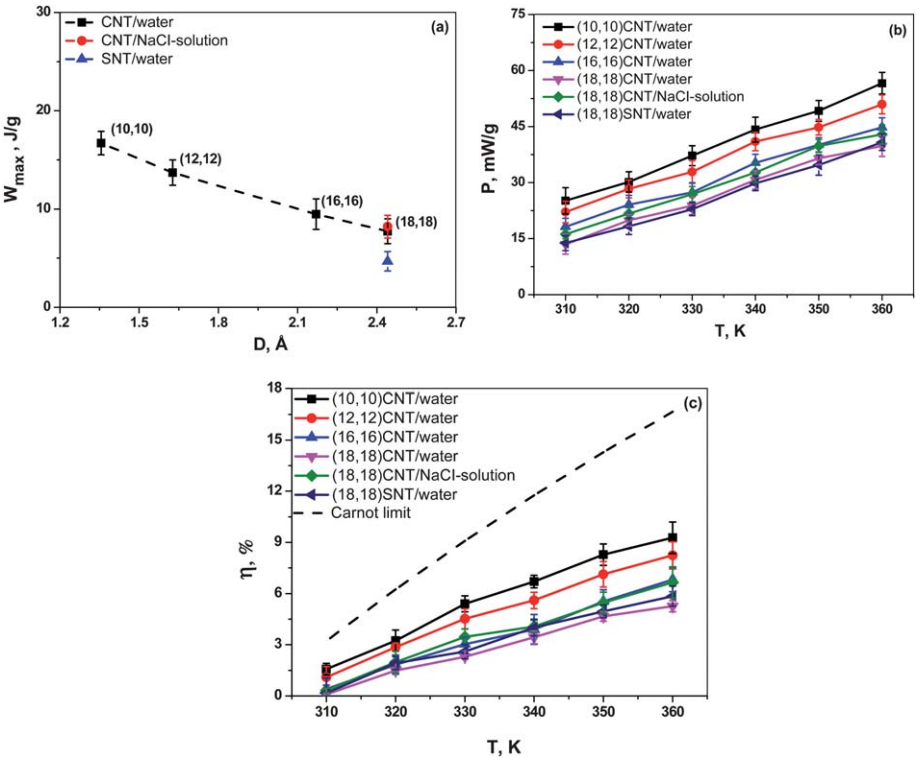

Fig. 7 (a) The maximum energy density, W_{max} per mass; here the error bar represents the small variation of W_{max} with respect to the temperature range considered; (b) the output power density, P per mass; (c) the thermal efficiency, η, of the thermo-actuation system.

In all numerical examples discussed above, the overall efficiency (calculated at t_0) is on the order of half of the Carnot efficiency, which indicates a decent performance of the proposed nanofluidic-based propulsion system.

4. Experimental verification

To validate the feasibility of the nanofluidic propulsion system, we performed a thermally controlled infiltration test on Zeolyst ZSM-5 zeolite. A series of treatments were carried out to control the degree of hydrophobicity of the pore surfaces, the details of which were given in ref. 31 The average pore diameter was about 1.26 nm with a standard deviation of 0.2 nm, and the overall nanopore volume was about 17%. About 1.0 g of zeolite was suspended in 7.0 g of de-ionized water. The suspension was sealed in a poly(methyl methacrylate) cylindrical cell by a steel piston (Fig. 8, inset). By compressing the piston which is controlled by a type 5580 Instron machine in a quasi-static manner, an external pressure was applied. The temperature was maintained by an Aldrich DigiTrol II Z28 water bath.

The typical sorption curves at elevated temperatures are shown in Fig. 8a. It clearly shows that the infiltration process took place when the applied pressure reached a critical pressure (*i.e.* P_{in}) and afterwards the infiltration plateau was formed. The width of the infiltration plateau is related to the specific pore volume, and the small slope of the infiltration stage is resulted from the slightly nonuniform pore size distribution; at the end of infiltration when the pores are filled up, the pressure increases again.

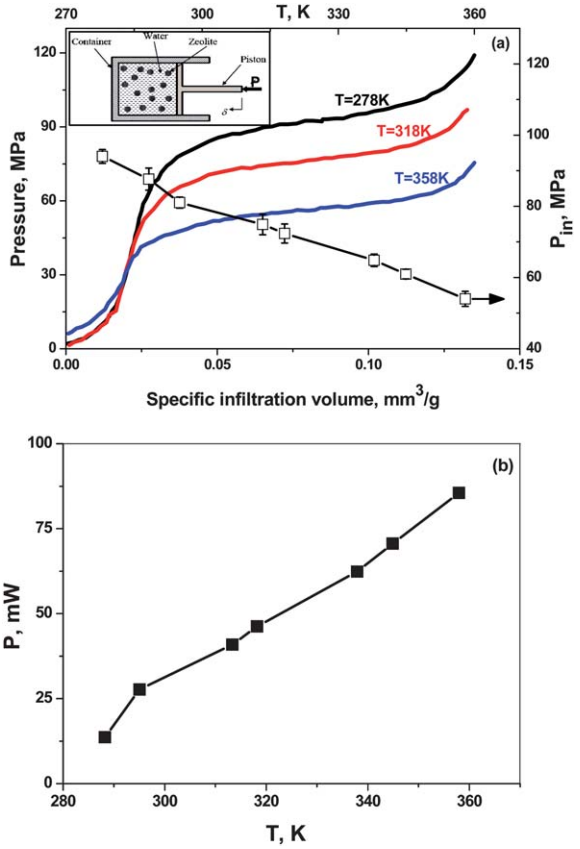

Fig. 8 (a) Experimental result of the sorption isotherm curves at different temperatures. The variation of the deduced infiltration pressure with temperature is also given. The experimental setup is illustrated at the corner inset; (b) variation of output power of the experimental thermal actuation system.

With the increase of temperature, P_{in} decreases almost linearly, which is qualitatively consistent with the simulation result in Fig. 2b. Such a temperature-sensitive infiltration behavior implies that if the applied pressure is kept as a constant just below the ambient $P_{in}^{T_0}$, as the temperature increases, the liquid would infiltrate spontaneously into nanopores, converting part of the thermal energy to mechanical work. Following this principle and the measurement of infiltration pressure in Fig. 8a, we let $T_0 = 278$ K as an illustrative example, and the measured power output, P, of such a conceptual thermal actuation system is given in Fig. 8b at elevated temperatures. It can be seen that the power output increases with temperature, qualitatively consistent with MD simulations. Note that due to several limitations such as the assumptions and parameterization adopted in the "idealized" computational model, as well as the specific pore structure used in experiment, the present comparison between simulation and experiment is rather qualitative, and more quantitative coordination will be pursued in future.

5. Concluding remarks

The thermally dependent infiltration behavior of nanofluids underpins high performance thermal actuation (or propulsion) and storage systems. Using MD simulations, we show that in a system containing a hydrophobic nanochannel and non-wetting liquid, with the increase of temperature or pore size, the critical infiltration pressure decreases, which is resulted from the reduced solid–liquid interfacial tension. The molecular mechanisms are elucidated through the thermal dependence of fundamental variables, including the radial density profile, contact angle, and surface tension of the confined liquid molecules. Moreover, the interactions between the thermal effect and pore size, pore phase, and liquid species are illustrated. It is found that the relative hydrophobicity is stronger with the employment of smaller pore, partially charged nanopore, or electrolyte.

Based on the thermally adjustable infiltration characteristics of liquids into nanopores, we put forward a conceptual design of a thermal actuation system. As the temperature is increased, the system becomes relatively more hydrophilic and thus the liquid could infiltrate the nanopores, converting part of the thermal energy into the excessive solid–liquid interfacial tension. When the temperature is reversed, the effective hydrophobicity enhances and the system volume increases as the liquid molecules are repelled out of nanopores. Through a constant pressure applied on the system, a significant mechanical work can be output with the volume reduction/expansion, similar to a thermal machine. The output power density and efficiency increase with the increase of temperature. For solid/liquid systems illustrated in the present study, the energy density is about 10 J g^{-1}, and the efficiency is on the same order of the Carnot efficiency. The parametric study shows that the system performance can be further improved by optimizing the pore size, solid phase, and liquid phase. A parallel thermally controlled infiltration experiment on a zeolite/water system is carried out, which qualitatively verifies the working principles and simulation findings.

We remark that the thermally controllable infiltration/defiltration process of liquids into/out of nanopores may also facilitate the development of high-density thermal storage devices. That is, the thermal energy may be effectively stored as the excessive liquid–solid interfacial energy, which can be on the order of 100 J g^{-1}. The detailed working mechanism and optimization will be reported elsewhere.

Acknowledgements

The work is supported by National Natural Science Foundation of China (50928601), World Class University program through the National Research Foundation of Korea (R32–2008–000–20042–0), Changjiang Scholar Program from Ministry of Education of China, DARPA (W91CRB-11-C-0112), and National Science Foundation (CMMI-0643726).

References

1 X. Chen, F. B. Surani, X. Kong, V. K. Punyamurtula and Y. Qiao, *Appl. Phys. Lett.*, 2006, **89**, 241918.
2 H. Daiguji, P. Yang, A. J. Szeri and A. Majumdar, *Nano Lett.*, 2004, **4**, 2315–2321.
3 F. H. J. van der Heyden, D. J. Bonthuis, D. Stein, C. Meyer and C. Dekker, *Nano Lett.*, 2006, **6**, 2232–2237.
4 Y. Qiao, V. K. Punyamurtual, A. Han and H. Lim, *J. Power Sources*, 2008, **183**, 403–405.
5 K. Artyushkova, A. L. Garcia and G. P. Lopez, *Microfluid. Nanofluid.*, 2010, **9**, 447–459.
6 A. L. Garcia, L. K. Ista, D. N. Petsev, M. J. O'Brien, P. Bisong, A. A. Mammoli, S. R. J. Brueck and G. P. Lopez, *Lab Chip*, 2005, **5**, 1271–1276.
7 J. Fu, R. Schoch, A. Stevens, S. Tannenbaum and J. Han, *Nat. Nanotechnol.*, 2007, **2**, 121–128.
8 R. Karnik, R. Fan, M. Yue, D. Li, P. Yang and A. A. Mammoli, *Nano Lett.*, 2005, **5**, 943–948.
9 W. H. Duan and Q. Wang, *ACS Nano*, 2010, **4**, 2338–2444.
10 C. Liu and Z. Li, *Phys. Rev. Lett.*, 2010, **105**, 174501.
11 M. J. Longhurst and N. Quirke, *Nano Lett.*, 2007, **7**, 3324–3328.
12 M. J. Longhurst and N. Quirke, *Nano Lett.*, 2007, **7**, 3324–3328.
13 Y. Qiao, V. K. Punyamurtula, A. Han, X. Kong and F. B. Surani, *Appl. Phys. Lett.*, 2006, **89**, 251905.
14 A. Han and Y. Qiao, *Appl. Phys. Lett.*, 2007, **91**, 173123.
15 Z. Jiao, X. Huang, N. T. Nguyen and P. Abgrall, *Microfluid. Nanofluid.*, 2008, **5**, 205–214.
16 N. T. Nguyen, T. H. Ting, Y. F. Yap, T. N. Wong and J. C. K. Chai, *Appl. Phys. Lett.*, 2007, **91**, 084102.
17 S. Plimpton, *J. Comput. Phys.*, 1995, **117**, 1–19.
18 J. Zhao, L. Liu, P. J. Culligan and X. Chen, *Phys. Rev. E: Stat., Nonlinear, Soft Matter Phys.*, 2009, **80**, 061206.
19 H. J. C. Berendsen, J. R. Grigera and T. P. Straatsma, *J. Phys. Chem.*, 1987, **24**, 6269–6271.
20 T. A. Andrea, W. C. Swope and H. C. Andersen, *J. Chem. Phys.*, 1984, **79**, 4576–4584.
21 T. Werder, J. H. Walther, R. L. Jaffe, T. Halicioglu and P. Koumoutsakos, *J. Phys. Chem. B*, 2003, **107**, 1345–1352.
22 J. Zhao, P. J. Culligan, Y. Qiao, Q. Zhou, Y. Li, M. Tak, T. Park and X. Chen, *J. Phys.: Condens. Matter*, 2010, **22**, 315301.
23 X. Chen, G. Cao, A. Han, V. K. Punyamurtula, L. Liu, P. J. Culligan, T. Kim and Y. Qiao, *Nano Lett.*, 2008, **8**, 2988–2992.
24 L. Liu, J. Zhao, C.-Y. Yin, P. J. Culligan and X. Chen, *Phys. Chem. Chem. Phys.*, 2009, **11**, 6520–6524.
25 T. Werder, J. H. Walther, R. L. Jaffe, T. Halicioglu, F. Noca and P. Koumoutsakos, *Nano Lett.*, 2001, **1**, 697–702.
26 L. Liu, J. Zhao, P. J. Culligan, Y. Qiao and X. Chen, *Langmuir*, 2009, **25**, 11862–11868.
27 L. Liu, X. Chen, W. Lu and Y. Qiao, *Phys. Rev. Lett.*, 2009, **102**, 184501.
28 J. K. Holt, H. G. Park, Y. M. Wang, M. Stadermann, A. B. Artyukhin, C. P. Grigoropoulos, A. Noy and O. Bakajin, *Science*, 2006, **312**, 1034–1037.
29 M. Wanunu and A. Meller, *Nano Lett.*, 2007, **7**, 1580–1585.
30 C. Dekker, *Nat. Nanotechnol.*, 2007, **2**, 209–215.
31 A. Han, W. Lu, T. Kim, V. K. Punyamurtula and Y. Qiao, *Smart Mater. Struct.*, 2009, **18**, 024005.